Journal of Zhejiang University-SCIENCE A (Applied Physics & Engineering) 2025 26(6):585-604
www.jzus.zju.edu.cn; www.springer.com/journal/11582
E-mail: jzus_a@zju.edu.cn

Regular paper

https://doi.org/10.1631/jzus.A2400462

Check for updates

Vibration characteristics of ballastless track and its effect on wheel–rail broadband dynamic interaction

Chaozhi MA[1], Liang GAO[2]✉, Pu WANG[3]✉, Bolun AN[4], Peng ZHOU[1], Mahantesh M NADAKATTI[5]

[1]*School of Mechanics and Civil Engineering, China University of Mining and Technology, Xuzhou 221116, China*
[2]*School of Civil Engineering, Beijing Jiaotong University, Beijing 100044, China*
[3]*Railway Engineering Research Institute, China Academy of Railway Sciences Corporation Limited, Beijing 100081, China*
[4]*Metals and Chemistry Research Institute, China Academy of Railway Sciences Corporation Limited, Beijing 100081, China*
[5]*Department of Mechanical Engineering, KLS Gogte Institute of Technology, Belagavi, India*

Abstract: The wheel–rail dynamic load (WRL) and its vibration energy transfer (VET) are foundational for studying ballastless track dynamics in high-speed railways. In this study, the higher-order modal parameters of track beds with different isolating layers were identified experimentally and a vehicle–track coupled dynamic model considering track bed broadband vibrations (TBBVs) was established. The WRL and its VET were investigated, and the contribution law as well as the influence mechanism of TBBVs on them was determined. The results showed the WRL and track bed vibration energy exhibited significant resonances, with more prominent high-frequency resonance peaks in the track bed vibration energy. TBBVs had a significant effect on low-frequency WRLs, and markedly influenced the VET across various frequency bands. Intense low-frequency and weak high-frequency intermodulation effects between the wheel–rail and track beds were observed. The effect of track bed vibrations can be disregarded when focusing on high-frequency WRLs above 200 Hz. Variations in the isolating layer stiffness have more significant effects on the track bed vibration energy than the WRL. Rational stiffness of the isolating layer should be selected to avoid mode-coupling resonance from track beds to the wheel–rail subsystem.

Key words: Ballastless track; Higher-order modal testing; Wheel–rail dynamic load (WRL); Vibration energy transfer (VET); Intermodulation effect; Rational stiffness

1 Introduction

Clarifying wheel–rail dynamic interactions is key to assessing the safety of train operations and studying the vibration and noise of railway systems. The wheel–rail dynamic load (WRL) at high speeds is intense and distributed in a broadband vibration zone of from 10 Hz to more than 1000 Hz under the excitation of the wheel polygon and rail corrugation (Zhai et al., 2020). Since the track directly bears and in turn affects the wheel–rail interaction, its reasonable modeling is the premise for accurate simulation of the wheel–rail broadband dynamic response. Most researchers simplify a sleeper or bed-per-span into a mass-spring system that is attached to the rail (Johansson and Nielsen, 2007; Sheng et al., 2016; Martínez-Casas et al., 2017; Mazilu, 2017; Blanco et al., 2018; Torstensson et al., 2019). A wheel–rail dynamic interaction model of a ballasted track has been established, and the broadband distribution characteristics of the wheel–rail vertical force have been well simulated.

Most of China's high-speed railway tracks are ballastless track structures, and complex flexible deformations of track beds need to be characterized. The Euler beam (Gupta and Degrande, 2010; Auersch and Said, 2021), elastic thin plate (Zhai et al., 2009), medium-thick plate theory (Luo et al., 2020; Zhai et al., 2023), finite element (El Kacimi et al., 2013; Xu and Zhai, 2019; Aggestam and Nielsen, 2020; Xu QY et al., 2022; Ren et al., 2024), and modal superposition (Zhu et al., 2017; Cai et al., 2019; Ling et al., 2020; Ma et al., 2023) have been proposed for modeling track beds, and a vehicle–ballastless track dynamic model considering bed or slab damage has

✉ Liang GAO, lgao@bjtu.edu.cn
Pu WANG, wpwp2012@yeah.net
Chaozhi MA, https://orcid.org/0000-0002-0718-6659

Received Sept. 28, 2024; Revision accepted Feb. 24, 2025; Crosschecked May 14, 2025

been developed (Luo et al., 2019; Yang et al., 2020; Miao et al., 2023). The WRLs under the wheel polygon, rail damage, and subgrade settlement have been analyzed based on vehicle–track coupled dynamic models (Chen et al., 2019; Liu et al., 2022; Zhang et al., 2023). Furthermore, the investigation of the transmission law of WRLs remains a prominent area of research interest. Ren et al. (2019) and Sarikavak and Goda (2022) studied the load transfer law of ballastless track and ballasted track for a high-speed railway. Zhang and Zhao (2020) investigated the dynamic transfer characteristics of vehicle loads for a double-block ballastless track. Zheng et al. (2020) tested the vibration transfer characteristics of a ballastless track on a long-span bridge. Gou et al. (2023) explored in detail the energy transmission law of ballastless track–bridge systems for high-speed railways. Sainz-Aja et al. (2020) studied the displacement and acceleration of the rail and twin block sleepers based on a detailed 3D slab track model, and clarified their transfer relationship. Hu et al. (2025) studied the deformation transmission law with tunneling beneath the pile-raft foundations. In addition, the environmental vibration caused by high-speed railways and urban rail transit and its transmission laws have been the subject of many studies (Kaynia et al., 2000; Takemiya, 2003; Ghangale et al., 2020; Xu LH et al., 2022; Wang et al., 2023; Ni et al., 2024). However, the broadband vibration characteristics of track beds have not been accurately considered in previous studies due to the lack of measurement results.

Ballastless track beds are multi-layer heterogeneous structures, composed of a slab, filling layer, isolating layer, and baseplate. The isolating layer is an important structural layer, and has many forms (Fig. 1). It is a 4-mm-thick geotextile in the general section. Instead of the geotextile, a cushion is used on long-span bridges and a vibration-damping layer in environmental protection areas. The stiffness per unit area of various isolating layers varies significantly, which leads to complex broadband vibration characteristics of track beds. Refined simulation of track bed broadband vibrations (TBBVs) remains inadequate due to the lack of measurement results. The contribution law and influence mechanism of broadband vibrations of track beds on the WRL and its vibration energy transfer (VET) have not been fully discussed theoretically.

The first task of this study was to establish a refined broadband vibration model of a ballastless track and its dynamic model coupled with the vehicle. The second task was to investigate the distribution characteristics of the WRL and its VET on the ballastless track. The third task was to study the effects of the broadband vibrations of track beds on the WRL and its VET, and to clarify the rational stiffness value of the isolating layer.

2 Measurement and modeling methods

Ballastless track broadband vibration characteristics were refined, simulated, and measured, and a vehicle–ballastless track dynamic interaction model was established.

2.1 Simulation and measurement of ballastless track broadband vibration characteristics

Taking the CRTS-III ballastless track as the main research object, a 3D finite element model of track beds was established to obtain the modal parameters according to the geometric dimensions (length, width, and height) and mechanical parameters (elastic modulus and density) of each structural layer (slab/filling layer/baseplate) (Fig. 2). The isolating layer and elastic foundation were considered to be equivalent to

Fig. 1 Track isolating layer for different scenarios: (a) geotextile in the general section; (b) cushion on a long-span bridge; (c) vibration-damping layer for environmental protection areas

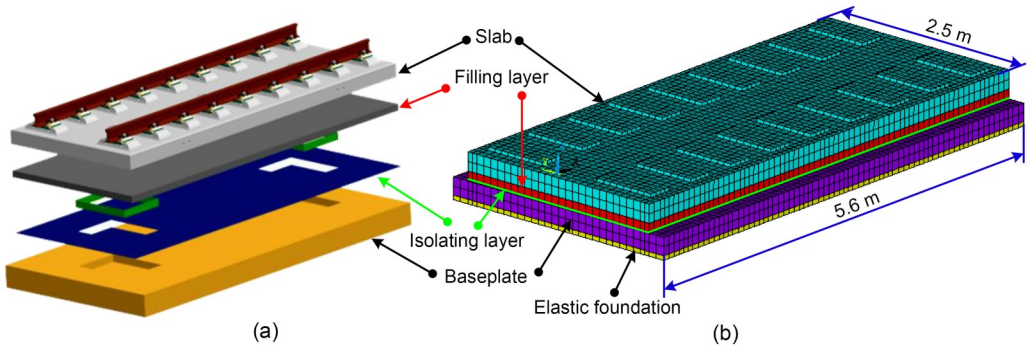

Fig. 2 CRTS-III ballastless track beds: (a) design model; (b) refined finite element model

solid elements with identical support stiffness. The conversion relationship between the elastic modulus E_g and support stiffness per unit area k_g is $E_g = k_g d_g$, where d_g is the structural layer thickness. In the vertical direction, each structural layer within track beds was bound and connected, with the bottom layer fully constrained. In the longitudinal direction, free boundaries were adopted at the slab joints due to the separation between the CRTS-III track beds.

The finite element mesh size altered the modal parameters, particularly those in the high-frequency modes. Fig. 3 shows that as the finite element mesh size decreases, the total modal order below 2500 Hz increases, and the frequency corresponding to the same high-order bending mode decreases. The modal order and modal frequency stabilize when the mesh size is taken as $c/6$ (i.e., 0.105 m), where c is the fastener node spacing. Therefore, the mesh size of the track beds was set to 1/6 of the fastener node spacing. The highest modal frequency was 2500 Hz, which covered the effect of the track bed vibrations on wheel–rail responses in the band of interest. A track bed is a high-frequency modal dense structure, and the total modal order in the range of 2500 Hz exceeds 200. For each track bed, there were 13248 elements and 16505 nodes.

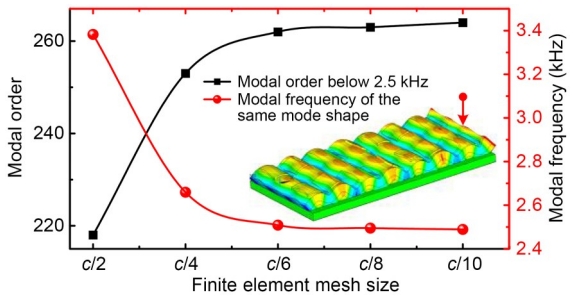

Fig. 3 Effect of finite element mesh size on modal parameters

Accurate analysis of modal parameters is the key to solving vehicle–ballastless track dynamic responses. Since the rail mass was much smaller than the track bed mass, its effect on the modal parameters of the track bed was negligible. For the CRTS-III ballastless track, a modal identification test for track beds was carried out using multi-input and multi-output methods (MIMO) on actual operating railway lines (Fig. 4). A force hammer was used to impact the excitation points, and the impulse response was collected by arranging several accelerometers at the response points. To obtain accurate multiple higher-order modes, the following conditions should be met: (1) a dense arrangement of excitation points (1/2 fastener node spacing settings, and cumulative 19×4=76 excitation points); (2) a multiple asymmetric arrangement of response points (seven response points throughout the entire track bed surface); (3) real-time determination of the coherence function of each response point (if less than 0.95, re-measure to ensure high-quality data).

Higher-order modes of track beds are not easily identified by field experiments. For high-speed railway track beds, low-order modes below 150 Hz have been identified experimentally (Zheng et al., 2023), and in this study higher-order modes beyond 800 Hz were identified. With the measurement results of the multimodal track bed parameters as the optimization objective, the elastic modulus and density of each structural layer of the track beds were modified, the elastic support role of the isolating layer was fully considered, and its support stiffness value was clarified. A refined broadband vibration model for track beds was established by integrating measurement results. The key mechanical and geometrical parameters of the track beds are listed in Table 1.

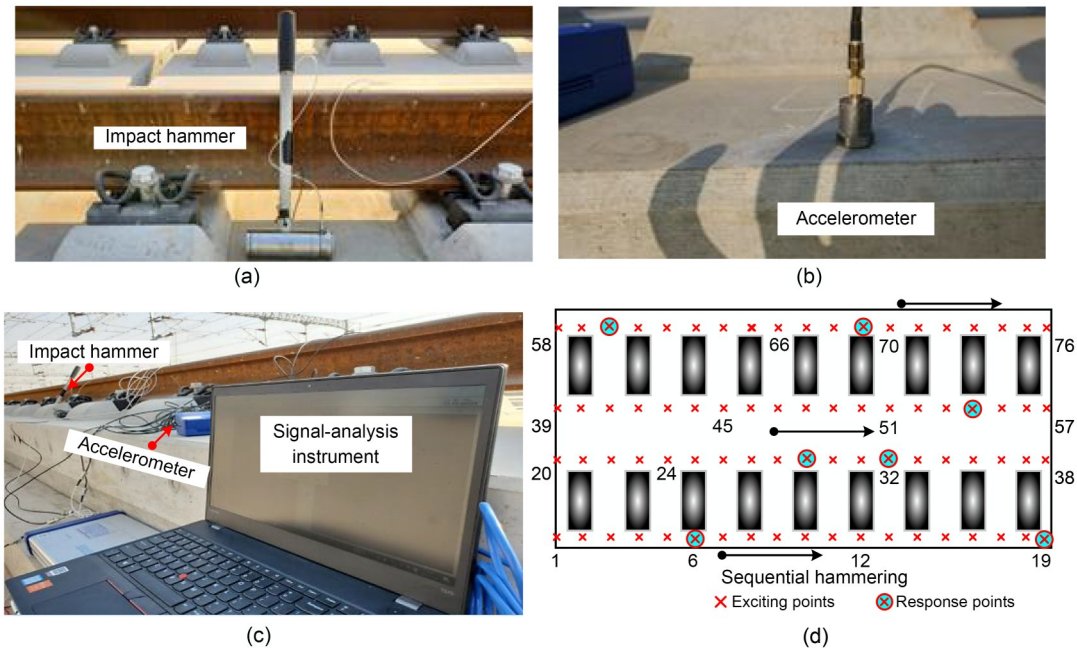

Fig. 4 Modal identification experiment for the CRTS-III ballastless track: (a) excitation devices; (b) accelerometer; (c) measurement scenario; (d) excitation input–response output point arrangement

Table 1 Key parameters of the vehicle and track system

Item	Parameter	Value
Track	Rail mass per unit length (kg)	60.64
	Elastic modulus of rail (GPa)	206
	Poisson's ratio of rail	0.3
	2nd moment of area about vertical direction of rail (m^4)	3.217×10^{-5}
	Vertical/lateral stiffness of fastener (MN/m)	30/50
	Vertical/lateral damping of fastener (kN·s/m)	30/50
	Fastener node spacing (m)	0.63
	Slab/filling layer/baseplate density (kg/m^3)	2450/2350/2350
	Slab/filling layer/baseplate modulus (GPa)	42.5/40.0/38.0
	Stiffness per unit area of geotextile/cushion/vibration-damping layer (MPa/m)	900/100/25
	Slab/filling layer/baseplate height (m)	0.21/0.10/0.20
	Slab/filling layer/baseplate width (m)	2.5/2.5/2.9
Vehicle	Carbody mass (kg)	34934
	Bogie mass (kg)	3300
	Wheelset mass (kg)	1750
	Primary suspension stiffness (MN/m)	1.1
	Primary suspension damping (kN·s/m)	10
	Secondary suspension stiffness (MN/m)	0.24
	Secondary suspension damping (kN·s/m)	20
	Wheelbase (m)	2.5
	Range between adjacent bogie wheels (m)	5
	Length between bogie centers (m)	17.5
	Vehicle speed (km/h)	300
	Wheel–rail adhesion/friction coefficient	0.04/0.17

Results of simulation and measurement comparisons for various track bed modes are shown in Fig. 5. The results verify the reliability of the track bed vibration model, as the maximum error between the simulated and measured modal frequencies was less than 5% for the same modal shape. Comparing Figs. 5a and 5b, it is evident that the modal frequency of the isolating layer with geotextile was higher than that of the isolating layer with cushion for the same modal shape.

2.2 Vehicle–ballastless track dynamic interaction model considering bed broadband vibrations

A vehicle–ballastless track dynamic interaction model considering bed broadband vibrations was established based on Zhai's vehicle–track coupled dynamics

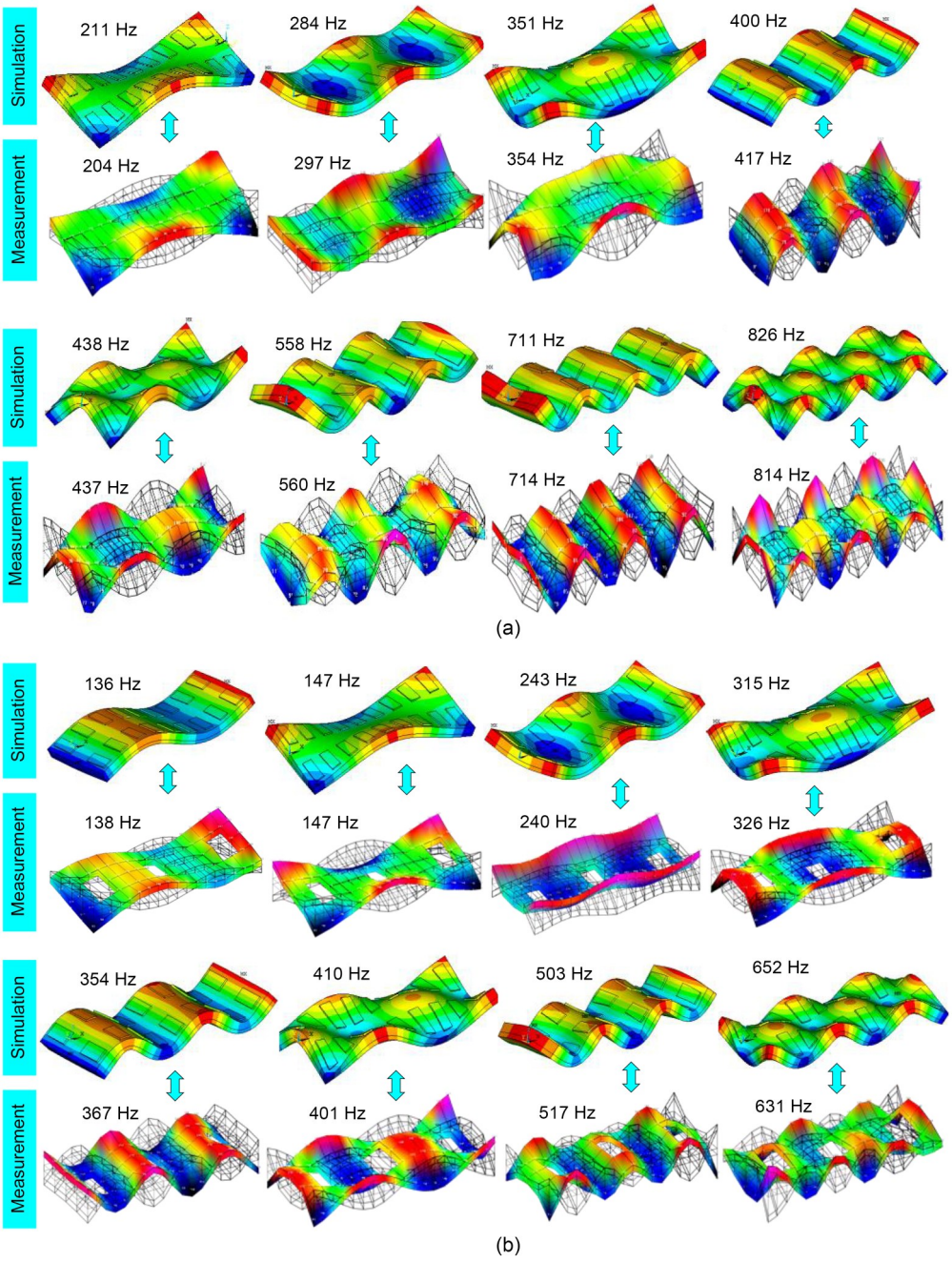

Fig. 5 Results of simulation and measurement comparisons for various track bed modes with different isolating layers: (a) isolating layer with geotextile; (b) isolating layer with cushion

theory (Zhai et al., 2009; Ling et al., 2014) (Fig. 6). Based on the substructure method, the model is composed of a double-vehicle subsystem, rail subsystem, fastener subsystem, and TBBV subsystem. A wheel–rail nonlinear contact model is used as the link between the vehicle and the rail.

As an infinite-strip periodic structure, the track generates strong vibrations within a finite length. For the track outside this range, the dynamic response is negligible. To improve efficiency within acceptable accuracy limits, a sliding window model (Song et al., 2018) was set up along the moving direction of the train. Only the track within the window was considered for computation. The sliding window can effectively reduce the high computational cost required to simulate the broadband dynamics of track beds.

2.2.1 Dynamic model for track beds

The modal superposition method was used to solve the vibration behavior of track beds. The track bed modal matrix $\boldsymbol{\Phi}_{\mathrm{s}}$ consists of two parts: the modes $\boldsymbol{\Phi}_{\mathrm{s}}^{\mathrm{mea}}$ below 900 Hz are verified from measurements, while modes $\boldsymbol{\Phi}_{\mathrm{s}}^{\mathrm{sim}}$ above 900 Hz are obtained using the refined finite element model. The track bed governing equations are as follows:

$$\boldsymbol{M}_{\mathrm{ss}}\boldsymbol{a}_{\mathrm{s}}+\boldsymbol{C}_{\mathrm{ss}}\boldsymbol{v}_{\mathrm{s}}+\boldsymbol{K}_{\mathrm{ss}}\boldsymbol{u}_{\mathrm{s}}=\boldsymbol{\Phi}_{\mathrm{s}}^{\mathrm{T}}\boldsymbol{F}_{\mathrm{sf}}, \tag{1}$$

$$\boldsymbol{d}_{\mathrm{s}}=\sum_{i=1}^{N_{\mathrm{s}}}\boldsymbol{\phi}_{\mathrm{s}}^{i}u_{\mathrm{s}}^{i}=\boldsymbol{\Phi}_{\mathrm{s}}\boldsymbol{u}_{\mathrm{s}},\quad \boldsymbol{\Phi}_{\mathrm{s}}=[\,\boldsymbol{\Phi}_{\mathrm{s}}^{\mathrm{mea}}\quad\boldsymbol{\Phi}_{\mathrm{s}}^{\mathrm{sim}}\,], \tag{2}$$

with

$$\frac{\boldsymbol{K}_{\mathrm{ss}}}{\boldsymbol{M}_{\mathrm{ss}}}=\mathrm{diag}[\,\omega_1^2\quad\omega_2^2\quad\cdots\quad\omega_{N_{\mathrm{s}}}^2\,],\quad \boldsymbol{C}_{\mathrm{ss}}=\alpha\boldsymbol{M}_{\mathrm{ss}}+\beta\boldsymbol{K}_{\mathrm{ss}}, \tag{3}$$

where $\boldsymbol{M}_{\mathrm{ss}}$, $\boldsymbol{C}_{\mathrm{ss}}$, and $\boldsymbol{K}_{\mathrm{ss}}$ are the generalized mass, damping, and stiffness matrices of the track beds, respectively; $\boldsymbol{a}_{\mathrm{s}}$, $\boldsymbol{v}_{\mathrm{s}}$, and $\boldsymbol{u}_{\mathrm{s}}$ are the generalized acceleration, velocity, and displacement vectors, respectively; $\boldsymbol{F}_{\mathrm{sf}}$ is the interaction force vector between the fastener and track beds; $\boldsymbol{d}_{\mathrm{s}}$ is the actual displacement vector; ω is the modal frequency; α and β are Rayleigh damping parameters of track beds; N_{s} is the reserved modal order; $\boldsymbol{\phi}_{\mathrm{s}}^{i}$ and u_{s}^{i} denote the ith mode and its participation factor, respectively.

A Boolean matrix $\boldsymbol{B}_{\mathrm{fs}}$ is used to select and arrange the track bed nodes connected with fasteners, and the dimensions of the generalized load matrix $\boldsymbol{\Phi}_{\mathrm{s}}^{\mathrm{T}}\boldsymbol{F}_{\mathrm{sf}}$ are unified:

$$\boldsymbol{\Phi}_{\mathrm{s}}^{\mathrm{T}}\boldsymbol{F}_{\mathrm{sf}}=\boldsymbol{\Phi}_{\mathrm{s}}^{\mathrm{T}}\boldsymbol{K}_{\mathrm{sf}}(\boldsymbol{u}_{\mathrm{f}}-\boldsymbol{B}_{\mathrm{fs}}\boldsymbol{\Phi}_{\mathrm{s}}\boldsymbol{u}_{\mathrm{s}})+\boldsymbol{\Phi}_{\mathrm{s}}^{\mathrm{T}}\boldsymbol{C}_{\mathrm{sf}}(\boldsymbol{v}_{\mathrm{f}}-\boldsymbol{B}_{\mathrm{fs}}\boldsymbol{\Phi}_{\mathrm{s}}\boldsymbol{v}_{\mathrm{s}}), \tag{4}$$

where $\boldsymbol{u}_{\mathrm{f}}$ and $\boldsymbol{v}_{\mathrm{f}}$ are the displacement and velocity vectors of the fastener iron chair, respectively; $\boldsymbol{K}_{\mathrm{sf}}$ and $\boldsymbol{C}_{\mathrm{sf}}$ are the stiffness and damping matrices provided by the fastener, respectively.

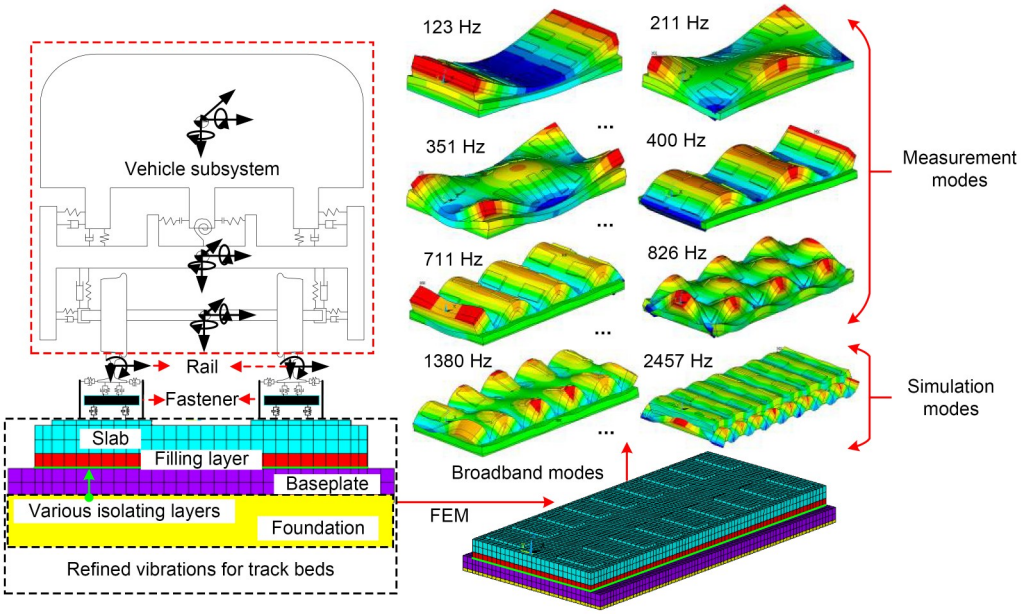

Fig. 6 Vehicle–ballastless track dynamic interaction model with refined consideration of TBBVs. FEM: finite element method

By substituting Eq. (4) into Eq. (1), the following equation is obtained:

$$\boldsymbol{M}_{\mathrm{ss}}\boldsymbol{a}_{\mathrm{s}}+(\boldsymbol{C}_{\mathrm{ss}}+\boldsymbol{\Phi}_{\mathrm{s}}^{\mathrm{T}}\boldsymbol{C}_{\mathrm{sf}}\boldsymbol{B}_{\mathrm{fs}}\boldsymbol{\Phi}_{\mathrm{s}})\boldsymbol{v}_{\mathrm{s}}+(\boldsymbol{K}_{\mathrm{ss}}+\boldsymbol{\Phi}_{\mathrm{s}}^{\mathrm{T}}\boldsymbol{K}_{\mathrm{sf}}\boldsymbol{B}_{\mathrm{fs}}\boldsymbol{\Phi}_{\mathrm{s}})\boldsymbol{u}_{\mathrm{s}}-\boldsymbol{\Phi}_{\mathrm{s}}^{\mathrm{T}}\boldsymbol{C}_{\mathrm{sf}}\boldsymbol{v}_{\mathrm{f}}-\boldsymbol{\Phi}_{\mathrm{s}}^{\mathrm{T}}\boldsymbol{K}_{\mathrm{sf}}\boldsymbol{u}_{\mathrm{f}}=\boldsymbol{0}. \quad (5)$$

2.2.2 Dynamic model for the vehicle–rail system

For the vehicle system, a 3D multi-body model comprising a two-section vehicle was established. The interactions among vehicles are simulated by linear or nonlinear spring-damper elements based on real constitutive relations. The vehicle dynamic equation can be described as follows:

$$\begin{bmatrix}\boldsymbol{M}_{\mathrm{vv}} & \\ & \boldsymbol{M}_{\mathrm{vv}}\end{bmatrix}\begin{bmatrix}\boldsymbol{a}_{\mathrm{v1}}\\ \boldsymbol{a}_{\mathrm{v2}}\end{bmatrix}+\begin{bmatrix}\boldsymbol{C}_{\mathrm{vv}} & \boldsymbol{C}_{\mathrm{cb}}\\ \boldsymbol{C}_{\mathrm{bc}} & \boldsymbol{C}_{\mathrm{vv}}\end{bmatrix}\begin{bmatrix}\boldsymbol{v}_{\mathrm{v1}}\\ \boldsymbol{v}_{\mathrm{v2}}\end{bmatrix}+\begin{bmatrix}\boldsymbol{K}_{\mathrm{vv}} & \boldsymbol{K}_{\mathrm{cb}}\\ \boldsymbol{K}_{\mathrm{bc}} & \boldsymbol{K}_{\mathrm{vv}}\end{bmatrix}\begin{bmatrix}\boldsymbol{u}_{\mathrm{v1}}\\ \boldsymbol{u}_{\mathrm{v2}}\end{bmatrix}=\begin{bmatrix}\boldsymbol{Q}_{\mathrm{wr1}}\\ \boldsymbol{Q}_{\mathrm{wr2}}\end{bmatrix}+\begin{bmatrix}\boldsymbol{Q}_{\mathrm{inv1}}\\ \boldsymbol{Q}_{\mathrm{inv2}}\end{bmatrix}, \quad (6)$$

where $\boldsymbol{M}_{\mathrm{vv}}$, $\boldsymbol{C}_{\mathrm{vv}}$, and $\boldsymbol{K}_{\mathrm{vv}}$ are the mass, damping, and stiffness matrices of a single-segment vehicle, respectively; $\boldsymbol{C}_{\mathrm{cb}}$ and $\boldsymbol{K}_{\mathrm{cb}}$ are the damping and stiffness matrices provided for the coupler buffer, respectively; $\boldsymbol{C}_{\mathrm{bc}}$ and $\boldsymbol{C}_{\mathrm{cb}}$, as well as $\boldsymbol{K}_{\mathrm{bc}}$ and $\boldsymbol{K}_{\mathrm{cb}}$, are symmetric matrices to each other; $\boldsymbol{a}_{\mathrm{v}}$, $\boldsymbol{v}_{\mathrm{v}}$, and $\boldsymbol{u}_{\mathrm{v}}$ are the vehicle acceleration, velocity, and displacement vectors, respectively; $\boldsymbol{Q}_{\mathrm{wr1}}$ and $\boldsymbol{Q}_{\mathrm{wr2}}$ are the wheel–rail nonlinear contact forces including the normal and creep forces, respectively; $\boldsymbol{Q}_{\mathrm{inv}}$ is the vehicle gravity.

A Timoshenko beam with periodic discrete support is used to simulate the rail vibrations. The rail dynamic equation is solved using the finite element method. The element displacement vector $\boldsymbol{u}_{\mathrm{r}}^{\mathrm{e}}(x,\,t)$ is expressed as:

$$\boldsymbol{u}_{\mathrm{r}}^{\mathrm{e}}(x,\,t)=\boldsymbol{N}_{\mathrm{r}}^{\mathrm{e}}(x)\left[[\boldsymbol{u}_{ri}^{\mathrm{e}}(t)]^{\mathrm{T}}\quad[\boldsymbol{u}_{rj}^{\mathrm{e}}(t)]^{\mathrm{T}}\right]^{\mathrm{T}}, \quad (7)$$

with

$$\begin{cases}\boldsymbol{u}_{ri}^{\mathrm{e}}=[\,u_{\mathrm{r}xi},\,u_{\mathrm{r}yi},\,u_{\mathrm{r}zi},\,\theta_{\mathrm{r}xi},\,\theta_{\mathrm{r}yi},\,\theta_{\mathrm{r}zi}\,]^{\mathrm{T}},\\ \boldsymbol{u}_{rj}^{\mathrm{e}}=[\,u_{\mathrm{r}xj},\,u_{\mathrm{r}yj},\,u_{\mathrm{r}zj},\,\theta_{\mathrm{r}xj},\,\theta_{\mathrm{r}yj},\,\theta_{\mathrm{r}zj}\,]^{\mathrm{T}},\end{cases} \quad (8)$$

where $\boldsymbol{N}_{\mathrm{r}}^{\mathrm{e}}(x)$ is the interpolation function; $\boldsymbol{u}_{ri}^{\mathrm{e}}$ and $\boldsymbol{u}_{rj}^{\mathrm{e}}$ are nodal displacements at end nodes i and j, respectively; t is the time; $u_{\mathrm{r}x}$, $u_{\mathrm{r}y}$, and $u_{\mathrm{r}z}$ represent the translational displacements in the x, y, and z directions; $\theta_{\mathrm{r}x}$, $\theta_{\mathrm{r}y}$, and $\theta_{\mathrm{r}z}$ represent the angles in the x, y, and z directions.

The dynamic governing equation of the rail is as follows:

$$\boldsymbol{M}_{\mathrm{rr}}\boldsymbol{a}_{\mathrm{r}}+\boldsymbol{C}_{\mathrm{rr}}\boldsymbol{v}_{\mathrm{r}}+\boldsymbol{K}_{\mathrm{rr}}\boldsymbol{u}_{\mathrm{r}}=\boldsymbol{Q}_{\mathrm{rw}}+\boldsymbol{Q}_{\mathrm{rf}}, \quad (9)$$

where $\boldsymbol{M}_{\mathrm{rr}}$, $\boldsymbol{C}_{\mathrm{rr}}$, and $\boldsymbol{K}_{\mathrm{rr}}$ are the mass, damping, and stiffness matrices of the rail itself, respectively; $\boldsymbol{a}_{\mathrm{r}}$, $\boldsymbol{v}_{\mathrm{r}}$, and $\boldsymbol{u}_{\mathrm{r}}$ are the rail acceleration, velocity, and displacement vectors, respectively; $\boldsymbol{Q}_{\mathrm{rw}}$ and $\boldsymbol{Q}_{\mathrm{rf}}$ are the wheel–rail load on the rail and the fastener support load, respectively.

A Boolean matrix $\boldsymbol{B}_{\mathrm{fr}}$ is used to select and arrange the rail nodes connected with fasteners, and $\boldsymbol{Q}_{\mathrm{rf}}$ can be expressed as follows:

$$\boldsymbol{Q}_{\mathrm{rf}}=\boldsymbol{K}_{\mathrm{rf}}(\boldsymbol{B}_{\mathrm{fr}}\boldsymbol{u}_{\mathrm{r}}-\boldsymbol{u}_{\mathrm{f}})+\boldsymbol{C}_{\mathrm{rf}}(\boldsymbol{B}_{\mathrm{fr}}\boldsymbol{v}_{\mathrm{r}}-\boldsymbol{v}_{\mathrm{f}}), \quad (10)$$

where $\boldsymbol{K}_{\mathrm{rf}}$ and $\boldsymbol{C}_{\mathrm{rf}}$ are stiffness and damping matrices provided for the fasteners, respectively.

By substituting Eq. (10) into Eq. (9), the following equation is obtained:

$$\boldsymbol{M}_{\mathrm{rr}}\boldsymbol{a}_{\mathrm{r}}+(\boldsymbol{C}_{\mathrm{rr}}-\boldsymbol{C}_{\mathrm{rf}}\boldsymbol{B}_{\mathrm{fr}})\boldsymbol{v}_{\mathrm{r}}+\boldsymbol{C}_{\mathrm{rf}}\boldsymbol{v}_{\mathrm{f}}+(\boldsymbol{K}_{\mathrm{rr}}-\boldsymbol{K}_{\mathrm{rf}}\boldsymbol{B}_{\mathrm{fr}})\boldsymbol{u}_{\mathrm{r}}+\boldsymbol{K}_{\mathrm{rf}}\boldsymbol{u}_{\mathrm{f}}=\boldsymbol{Q}_{\mathrm{rw}}. \quad (11)$$

For the fastener system, the dynamic governing equation was adopted from Ma et al. (2023).

For the wheel–rail contact model, the wheel–rail contact is the core bond between the vehicle and track systems. The normal and tangential contacts are solved by the Kik-Piotrowski non-Hertz algorithm (Piotrowski and Kik, 2008) and the FastSim algorithm (Kalker, 1982), respectively. The excitation sources of the vehicle–track system are the surface roughness of the rail or wheel and the random irregularity of the track. The wheel–rail excitation comprises the measured irregularity of China's high-speed railway lines and the wheel–rail surface roughness (the short-wavelength irregularity). The wheel–rail surface roughness adopts the Sato union roughness spectrum (Sato, 1977).

$$Q_{\mathrm{nc}}=\frac{\pi E\delta}{2(1-\mu^2)}\frac{\displaystyle\int_{y_{\mathrm{r}}}^{y_{\mathrm{l}}}\int_{-x_{\mathrm{l}}}^{x_{\mathrm{l}}}\sqrt{x_{\mathrm{l}}^2(y)-x^2}\,\mathrm{d}x\mathrm{d}y}{\displaystyle\int_{y_{\mathrm{r}}}^{y_{\mathrm{l}}}\int_{-x_{\mathrm{l}}}^{x_{\mathrm{l}}}\frac{\sqrt{x_{\mathrm{l}}^2(y)-x^2}}{\sqrt{x^2+y^2}}\mathrm{d}x\mathrm{d}y}, \quad (12)$$

$$p_{\mathrm{n}}(x,y)=\frac{N\sqrt{2R_{\mathrm{w}}\varepsilon\delta}}{\int_{y_{\mathrm{r}}}^{y_{\mathrm{l}}}\int_{-x_{\mathrm{l}}}^{x_{\mathrm{l}}}\sqrt{x_{\mathrm{l}}^2(y)-x^2}\,\mathrm{d}x\mathrm{d}y}\frac{\sqrt{x_{\mathrm{l}}^2(y)-x^2}}{x_{\mathrm{l}}(0)},\tag{13}$$

$$\delta=\frac{z_{\mathrm{c}}^{\mathrm{wheel}}-z_{\mathrm{c}}^{\mathrm{rail}}-z_0}{\cos(\theta+\varphi)},\tag{14}$$

where Q_{nc} is the normal contact force; $p_{\mathrm{n}}(x,y)$ is the contact pressure at coordinate (x,y); E is the elastic modulus and μ is Poisson's ratio; δ is the virtual penetration; ε is the correction factor; R_{w} is the wheel rolling radius; x_{l}, y_{l}, and y_{r} denote the edges of the interpenetration area; $z_{\mathrm{c}}^{\mathrm{wheel}}$ and $z_{\mathrm{c}}^{\mathrm{rail}}$ are the vertical displacement of the wheel and rail at the contact patch, respectively; z_0 is the wheel–rail surface roughness; θ is the contact angle and φ is the relative roll angle of the wheel–rail tread.

The governing equations of the vehicle–ballastless track system are obtained by combining the dynamic equations of the vehicle, rail, fastener, and track beds.

$$\begin{bmatrix}\boldsymbol{M}_{\mathrm{tt}}&&&\\&\boldsymbol{M}_{\mathrm{rr}}&&\\&&\boldsymbol{M}_{\mathrm{ff}}&\\&&&\boldsymbol{M}_{\mathrm{ss}}\end{bmatrix}\begin{bmatrix}\boldsymbol{a}_{\mathrm{t}}\\\boldsymbol{a}_{\mathrm{r}}\\\boldsymbol{a}_{\mathrm{f}}\\\boldsymbol{a}_{\mathrm{s}}\end{bmatrix}+\begin{bmatrix}\boldsymbol{C}_{\mathrm{tt}}&&&\\&\boldsymbol{C}_{\mathrm{rr}}-\boldsymbol{C}_{\mathrm{rf}}\boldsymbol{B}_{\mathrm{fr}}&\boldsymbol{C}_{\mathrm{rf}}&\\&\boldsymbol{C}_{\mathrm{fr}}&\boldsymbol{C}_{\mathrm{ff}}&-\boldsymbol{C}_{\mathrm{fs}}\boldsymbol{\Phi}_{\mathrm{s}}\\&&-\boldsymbol{\Phi}_{\mathrm{s}}^{\mathrm{T}}\boldsymbol{C}_{\mathrm{sf}}&\boldsymbol{C}_{\mathrm{ss}}+\boldsymbol{\Phi}_{\mathrm{s}}^{\mathrm{T}}\boldsymbol{C}_{\mathrm{sf}}\boldsymbol{B}_{\mathrm{fs}}\boldsymbol{\Phi}_{\mathrm{s}}\end{bmatrix}\begin{bmatrix}\boldsymbol{v}_{\mathrm{t}}\\\boldsymbol{v}_{\mathrm{r}}\\\boldsymbol{v}_{\mathrm{f}}\\\boldsymbol{v}_{\mathrm{s}}\end{bmatrix}+\begin{bmatrix}\boldsymbol{K}_{\mathrm{tt}}&&&\\&\boldsymbol{K}_{\mathrm{rr}}-\boldsymbol{K}_{\mathrm{rf}}\boldsymbol{B}_{\mathrm{fr}}&\boldsymbol{K}_{\mathrm{rf}}&\\&\boldsymbol{K}_{\mathrm{fr}}&\boldsymbol{K}_{\mathrm{ff}}&-\boldsymbol{K}_{\mathrm{fs}}\boldsymbol{\Phi}_{\mathrm{s}}\\&&-\boldsymbol{\Phi}_{\mathrm{s}}^{\mathrm{T}}\boldsymbol{K}_{\mathrm{sf}}&\boldsymbol{K}_{\mathrm{ss}}+\boldsymbol{\Phi}_{\mathrm{s}}^{\mathrm{T}}\boldsymbol{K}_{\mathrm{sf}}\boldsymbol{B}_{\mathrm{fs}}\boldsymbol{\Phi}_{\mathrm{s}}\end{bmatrix}\begin{bmatrix}\boldsymbol{u}_{\mathrm{t}}\\\boldsymbol{u}_{\mathrm{r}}\\\boldsymbol{u}_{\mathrm{f}}\\\boldsymbol{u}_{\mathrm{s}}\end{bmatrix}=\begin{bmatrix}\boldsymbol{Q}_{\mathrm{wr}}+\boldsymbol{Q}_{\mathrm{int}}\\\boldsymbol{Q}_{\mathrm{rw}}\\\boldsymbol{0}\\\boldsymbol{0}\end{bmatrix},\tag{15}$$

where $\boldsymbol{M}_{\mathrm{tt}}$, $\boldsymbol{C}_{\mathrm{tt}}$, and $\boldsymbol{K}_{\mathrm{tt}}$ are the mass, damping, and stiffness matrices of two-section vehicles, respectively; $\boldsymbol{a}_{\mathrm{t}}$, $\boldsymbol{v}_{\mathrm{t}}$, and $\boldsymbol{u}_{\mathrm{t}}$ are the acceleration, velocity, and displacement vectors of two-section vehicles, respectively; $\boldsymbol{M}_{\mathrm{ff}}$, $\boldsymbol{C}_{\mathrm{ff}}$, and $\boldsymbol{K}_{\mathrm{ff}}$ are the mass, damping, and stiffness matrices of the fastener system, respectively; $\boldsymbol{C}_{\mathrm{fs}}$ and $\boldsymbol{C}_{\mathrm{sf}}$, as well as $\boldsymbol{K}_{\mathrm{fs}}$ and $\boldsymbol{K}_{\mathrm{sf}}$, are symmetric matrices to each other; $\boldsymbol{Q}_{\mathrm{wr}}$ and $\boldsymbol{Q}_{\mathrm{int}}$ are the wheel–rail nonlinear contact force and gravity of two-section vehicles.

2.3 Track dynamic response measurement and model validation

The model's reliability across different frequency bands was validated through on-site dynamic response measurements of the track. The rail and track bed dynamic responses for general ballastless tracks were tested on-site. The mid-span rail acceleration and fastener position track bed acceleration were obtained through simulation. The proposed vehicle–ballastless track coupled model was validated by comparing simulated and measured data (Figs. 7–9). Note that low-pass filtering below 1500 Hz was performed on the measured and simulated data.

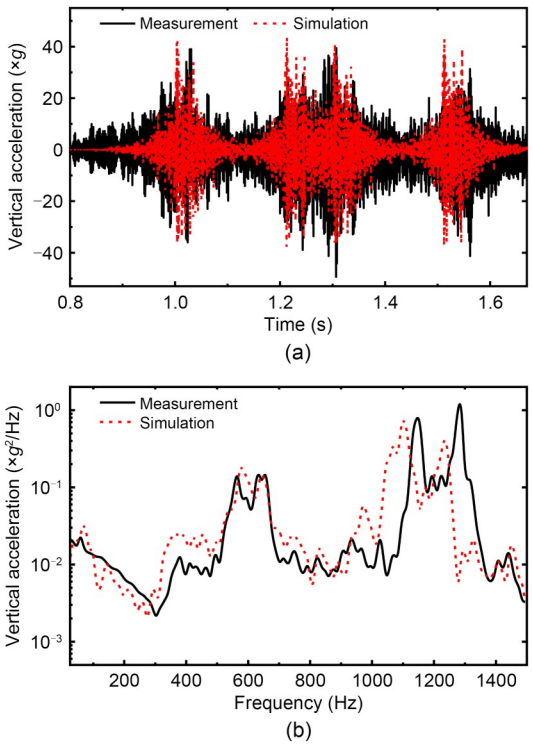

Fig. 7 Simulation and measurement of rail acceleration: (a) time domain; (b) frequency domain. *g* is the acceleration of gravity

As shown in Figs. 7 and 8, the simulated and measured results of rail and track bed accelerations were consistent in terms of both the time-domain and frequency-domain distributions. From Fig. 7b, two resonance peaks appear at 550–650 and 1050–1250 Hz for the rail acceleration. Combined with the results of

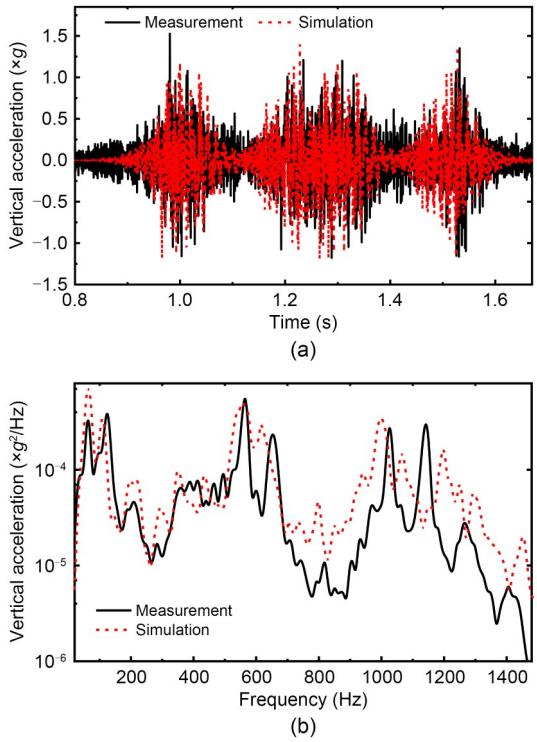

Fig. 8 Simulation and measurement of track bed acceleration: (a) time domain; (b) frequency domain

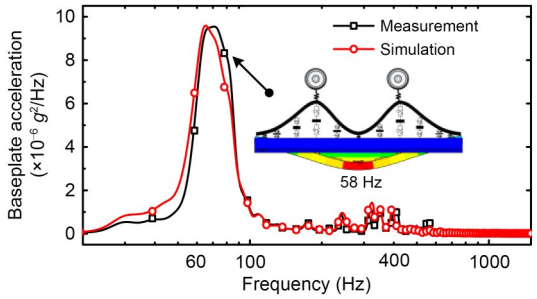

Fig. 9 Simulation and measurement of the baseplate acceleration for the vibration-damping track

the analysis of WRL in Section 3.2, these resonances are caused by the rail's 3rd-order bending and pinned-pinned vibration modes between bogie wheels, respectively. In Fig. 8b, the track bed acceleration shows significant resonances at 30–100, 550–650, and 900–1100 Hz. The low-frequency resonance at 30–100 Hz is generated by the P2 resonance mode and low-order modes of the track bed. The P2 resonance mode is the equal-amplitude, in-phase vibration mode of the wheel relative to the rail.

To verify the accuracy of the track bed model with a vibration-damping isolating layer, Fig. 9 shows the simulation and measurement results of the baseplate acceleration for the vibration-damping track. The vehicle operating speed on this track test section is 250 km/h. The simulation and measurement results of the baseplate acceleration are in good agreement. In addition, setting a vibration-damping layer causes the baseplate acceleration to resonate near 60 Hz, which is known from Fig. 21 to be caused by the coupled resonance of the wheel–rail P2 resonance mode and the track bed's 1st-order bending mode.

In general, the ballastless track model is doubly validated in time and frequency within 1500 Hz based on the rectification of higher-order modal measurements and the verification of broadband dynamic response measurements.

3 Simulation results

In this section, we first introduce the indicators for evaluating wheel–rail broadband dynamic interactions. Then, taking the CRTS-III ballastless track as an example, the WRL and its VET characteristics on track beds are simulated.

3.1 Indicators for evaluating dynamic interaction between wheel–rail and track beds

The dynamic interaction between the wheel–rail and track beds considers the WRL and its vibration transfer to the track beds. The vibration transfer between the wheel–rail and track beds is a diffusion process from point (wheel–rail contact point) to surface (track bed surface), as shown in Fig. 10. To evaluate the VET on the ballastless track, the power flow method (Hussein and Hunt, 2006; Clot et al., 2014; Li et al., 2016) has been widely adopted. Therefore, wheel–rail force and power indicators were used to measure the dynamic interaction between the wheel–rail and track beds.

The impact power ($E^{\mathrm{t}}_{\mathrm{impact}}$) input to the track is considered, which can be expressed as the product of the wheel–rail dynamic contact force and the contact-point velocity caused by the track dynamic deformation. Considering that the vehicle is operating on a straight track, the wheel–rail vertical contact force is much greater than the lateral force. The impact power can be expressed as:

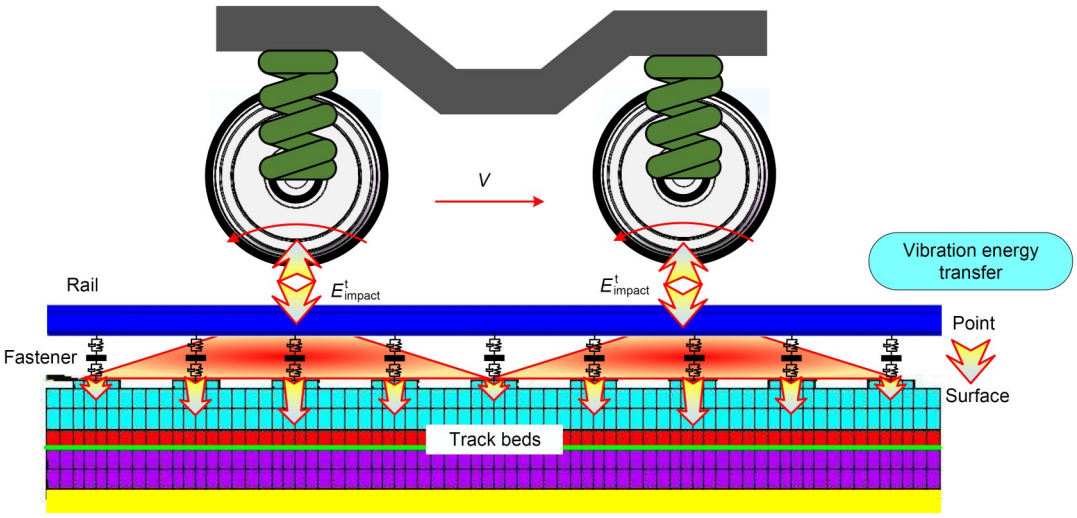

Fig. 10 Schematic diagram of the WRL and its VET on the track

$$E^{t}_{impact}=F_z\frac{du^{t}_{z}}{dt}, \tag{16}$$

where F_z is the wheel–rail vertical contact force and u^{t}_{z} is the vertical deflection of the contact point caused by the track dynamic deflection.

The energy transferred to the track beds (E^{s}_{impact}), i.e., the track bed vibration energy, can be expressed as the sum of the product of the fastener force acting on the track beds and the corresponding track bed node velocity within the wheel load impact range. Owing to the large amplitude variation in the entire frequency range, the vibration level (E^{s}_{VL}) is used for convenience.

$$E^{s}_{impact}=\sum_{i=1}^{N_f}F^{s}_{i}\frac{du^{s}_{zi}}{dt}, \tag{17}$$

$$E^{s}_{VL}=10\lg\left(\frac{E^{s}_{impact}}{E_0}\right), \tag{18}$$

where F^{s}_{i} is the fastener force acting on track beds; u^{s}_{zi} is the track bed node deflection; N_f is the total number of load-bearing fasteners under the wheel load; E_0 is a reference value, taken as 1×10^{-12} W.

E_{TL} is used to evaluate the degree of energy transmission loss from the wheel–rail to the track beds.

$$E_{TL}=10\lg\left(\frac{E^{t}_{impact}}{E_0}\right)-10\lg\left(\frac{E^{s}_{impact}}{E_0}\right)=10\lg\left(\frac{E^{t}_{impact}}{E^{s}_{impact}}\right). \tag{19}$$

3.2 Wheel–rail broadband dynamic load characteristics

The WRL within the 1500 Hz broadband was studied (Fig. 11).

As shown in Fig. 11, there are significant resonances for the WRL, in which the impact power resonates around 45, 600, and 1000 Hz, and the vertical force resonates around 45, 360, 600, and 1000 Hz. Furthermore, the 45 Hz resonance belongs to the low-frequency range, and its resonance peak is the most significant in the entire frequency range. The other three resonances belong to the high-frequency range. In addition, unlike for the vertical force, there is no 2nd resonance for the impact power.

We believe that the P2 resonance and rail's 2nd and 3rd-order bending and pinned-pinned vibration modes between the bogie wheels result in wheel–rail coupled resonances around 45, 360, 600, and 1000 Hz, respectively (Ma et al., 2021). The absence of the 2nd resonance for impact power is determined by rail's 2nd-order bending modal shape. For this mode, the wheels are located exactly at the wave node of the rail bending mode, so the rail dynamic deflection and velocity at the wheel–rail contact point will be minimal. As a result, when this mode is excited, an impact power resonating near 360 Hz will not be generated.

3.3 Vibration energy transfer characteristics for a ballastless track

The impact power transmitted to track beds, i.e., the track bed vibration energy, is solved, and the VET

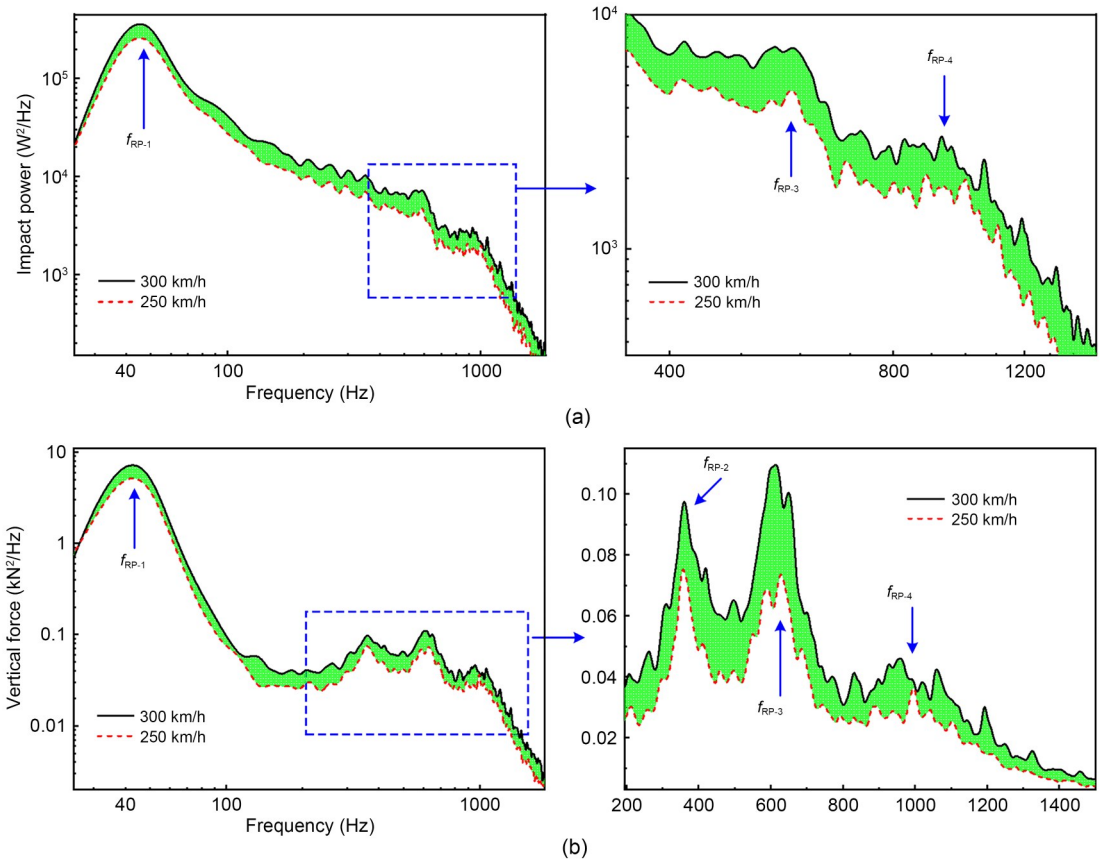

Fig. 11 WRL characteristics: (a) impact power; (b) vertical force. $f_{RP\text{-}i}$ denotes the *i*th resonance band

characteristics from the wheel–rail to track beds are determined, as shown in Fig. 12.

Fig. 12a shows that the impact power from the wheel–rail system to the track beds decreases from 4175 to 104 W, and decays to 1/40. The wheel–rail impact energy is 40 times greater than the track bed vibration energy. The track bed vibration energy is greatly weakened due to the significant vibration-isolating effects of track fasteners.

Fig. 12b shows that the impact power transmitted to the track beds resonates significantly at 40–80, 530–630, and 850–1000 Hz. Moreover, the energy transmission loss from the wheel–rail system to the track beds is 18.5, 18.6, and 20.7 dB at 45, 580, and 950 Hz, respectively. Overall, the energy transmission loss tends to increase with increasing frequency, indicating that the high-frequency energy is more difficult to transfer from the wheel–rail system to the track beds compared to the low-frequency energy. Specifically, when the wheel–rail impact undergoes high-frequency resonances, the track bed vibration energy exhibits more prominent resonance peaks, while the

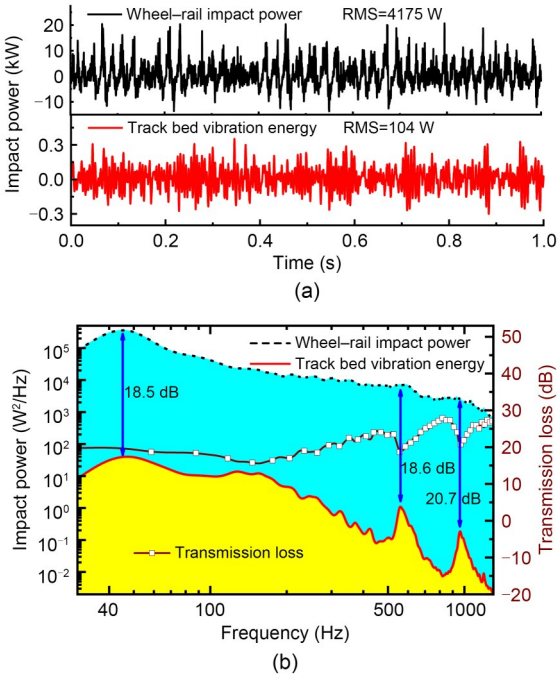

Fig. 12 VET characteristics from the wheel–rail system to the track beds: (a) time domain; (b) frequency domain. RMS is the root mean square value

energy transmission losses exhibit valleys. The wheel–rail impact energy at resonant frequency bands is more prone to transfer to the track beds than that at adjacent non-resonant frequency bands.

4 Discussion

The contribution law of TBBVs to the WRL and its VET was studied, and the influence mechanism of TBBVs on wheel–rail dynamics was revealed from the perspective of the intermodulation effect. Finally, the rational stiffness of the isolating layer is discussed from the viewpoint of avoiding mode-coupling resonance between subsystems. Unless otherwise specified, the track bed structure in this section is the CRTS-III ballastless track bed.

4.1 Influence law of track bed vibration on wheel–rail dynamic interaction

The variations of the track bed type and the material of the isolating layer (geotextile, cushion, or vibration-damping layer) significantly change the broadband vibration characteristics of track beds. This section focuses on the effects of the TBBVs on the WRL and its VET.

4.1.1 Track bed type

The CRTS-III track slab and double-block track bed are ballastless track structures commonly used for high-speed railways in China. Table 2 lists the typical higher-order modal characteristics of these two track structures. The modal parameters of the two track structures differ: the modal frequency of the CRTS-III track slab is significantly higher than that of the double-block track bed under the same modal shape. The WRL and its energy transfer under different track bed structures were simulated by introducing the modal parameters of these two track beds into the vehicle–track dynamic interaction model (Figs. 13 and 14).

Fig. 13 shows that the difference in the WRL between CRTS-III track slab and double-block track bed is not significant, even though the modal differences between these two track structures are significant. The double-block track bed has less vibration energy and higher energy transmission losses below 400 Hz than the CRTS-III track slab (Fig. 14). We infer that the vibration energy below 400 Hz is not easily transmitted from the wheel–rail system to the double-block track bed.

In addition, when the two track structures undergo high-frequency resonance, the vibration energy of the double-block track bed is enhanced at 580 Hz and

Table 2 Comparison of modal parameters between the CRTS-III track slab and double-block track bed

Parameter type	Description	
	CRTS-III track slab	Double-block track bed
Structural parameter	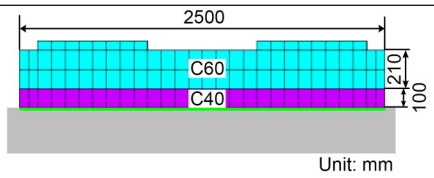	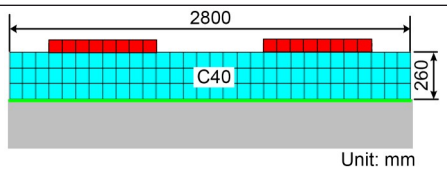
9th-order co-direction bending mode	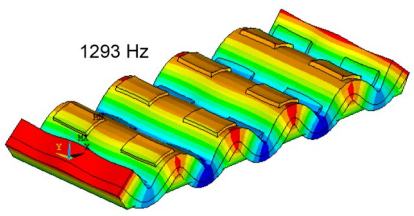	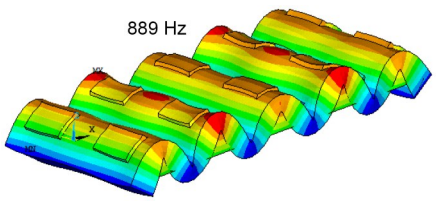
9th-order reverse bending mode	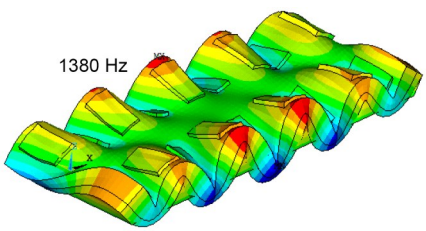	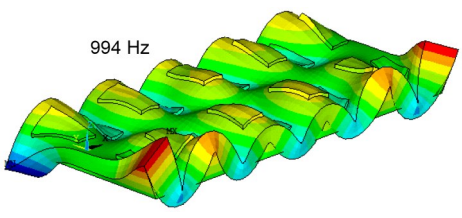

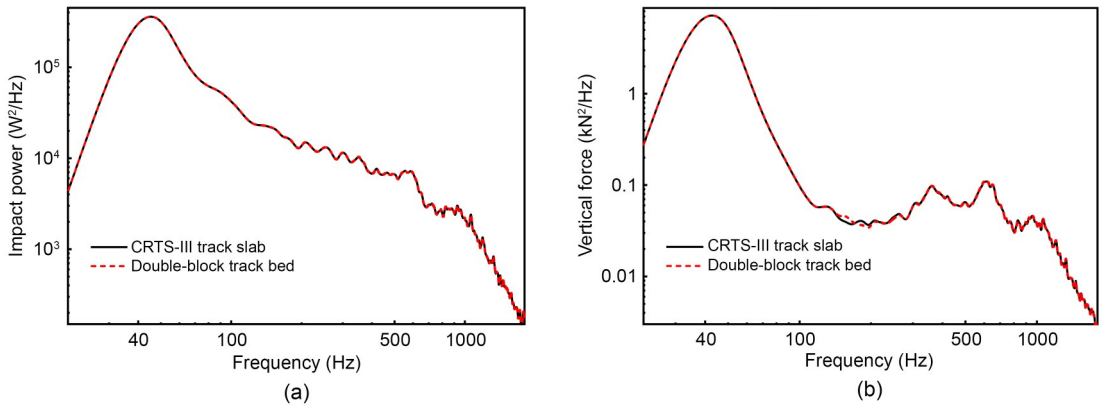

Fig. 13 Influence of the track bed type on the WRL: (a) impact power; (b) vertical force

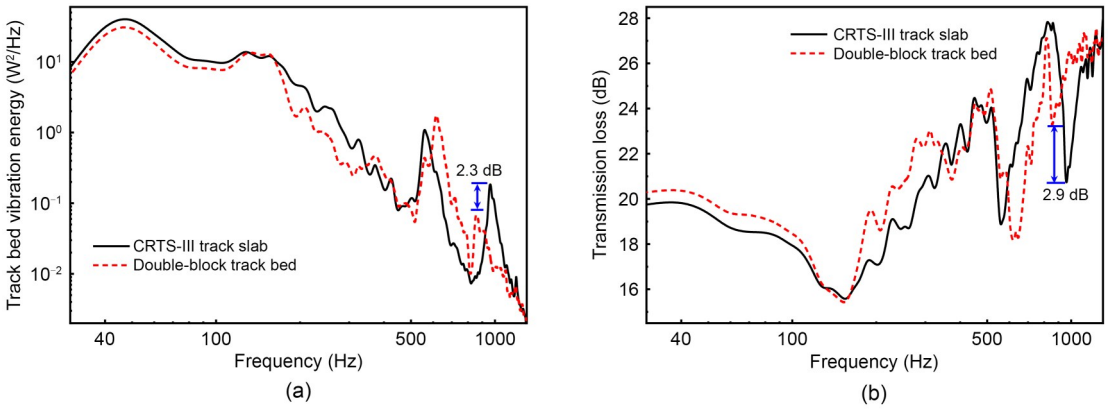

Fig. 14 Influence of the track bed type on wheel–rail VET: (a) track bed vibration energy; (b) energy transmission loss

significantly weakened at 950 Hz. When the track resonates at 950 Hz, the rail exhibits pinned-pinned resonance, while the double-block track bed exhibits the 9th-order bending resonance (Fig. 15). The rail and the track bed form a coupled resonance with a phase difference of $\pi/2$, which is responsible for the significant weakening of the vibration energy. In general, the change in broadband vibration characteristics of the ballastless track bed has little influence on the WRL, but significantly contributes to its VET.

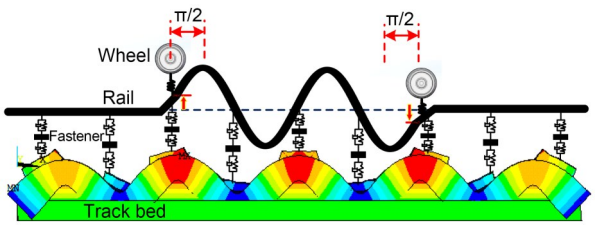

Fig. 15 Coupled resonance of pinned-pinned vibration of rail and 9th-order bending mode of track bed

4.1.2 Isolating cushion on a long-span bridge

To coordinate the deformation and ensure the smoothness of a ballastless track on a long-span bridge, an isolating cushion is laid underneath the track bed. The stiffness of the isolating cushion is 100 MPa/m. Laying isolating cushions changes the broadband vibration characteristics of the track bed itself. The influences of laying isolating cushions on the WRL and its VET are shown in Figs. 16 and 17, respectively.

Fig. 16 shows that laying isolating cushions weakens the wheel–rail P2 resonance energy at 40–50 Hz but has little effect on the high-frequency wheel–rail interaction above 200 Hz. Fig. 17 shows that laying isolating cushions influences the energy transfer from the wheel–rail system to the track beds across the entire frequency band, and the contribution is more significant below 200 Hz. Specifically, laying isolating cushions aggravates the track bed vibrations by about 10 dB, reduces the energy transmission loss

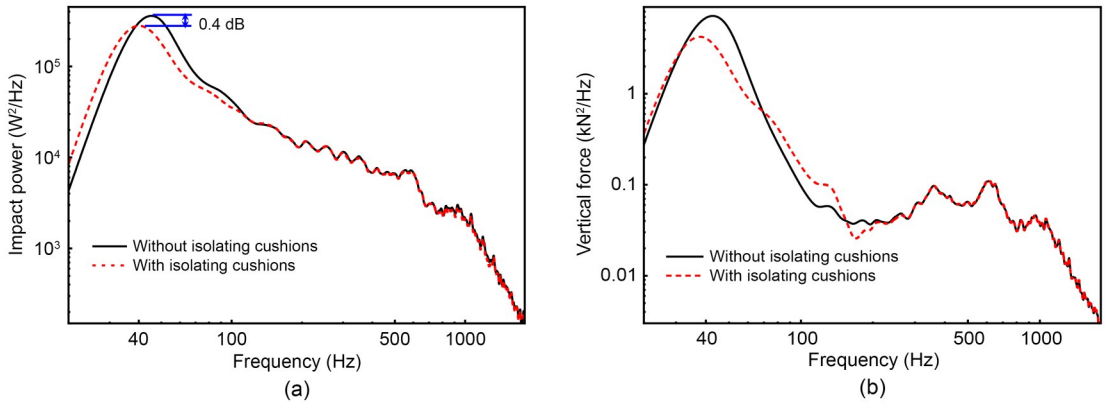

Fig. 16 Influence of laying isolating cushions on the WRL: (a) impact power; (b) vertical force

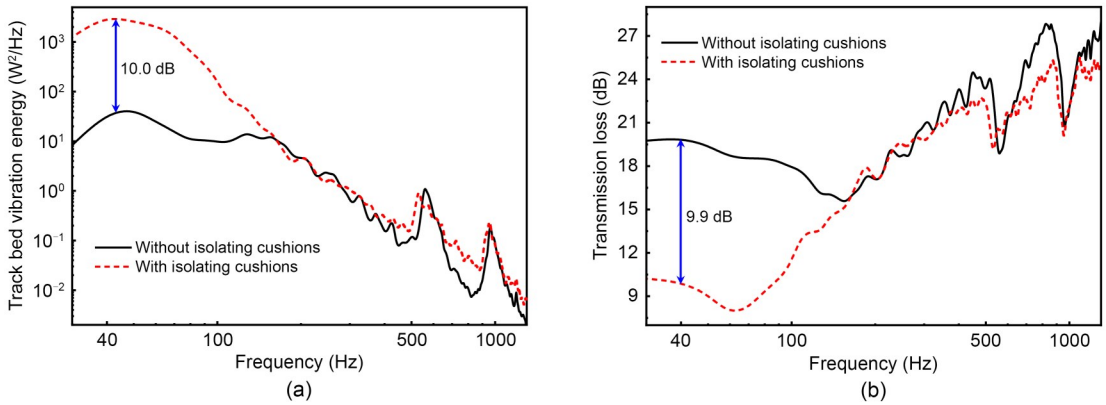

Fig. 17 Influence of laying isolating cushions on the wheel–rail VET: (a) track bed vibration energy; (b) energy transmission loss

significantly, and makes the high-frequency energy distribution of the track beds more uniform. We conclude that laying isolating cushions slightly attenuates the wheel–rail impacts and significantly aggravates the track bed vibrations.

4.1.3 Vibration-damping layer for environmental protection areas

A vibration-damping ballastless track is often installed in environmental protection areas, i.e., the vibration-damping layer is laid under the track beds to form floating track structures. The stiffness of the vibration-damping layer is 25 MPa/m. The effects of the vibration-damping track on the WRL and its energy transfer are shown in Figs. 18 and 19, respectively.

Fig. 18 shows that the vibration-damping layer significantly reduces the wheel–rail impacts below 200 Hz, whereas it has a limited effect on the high-frequency wheel–rail interactions. The laying of a vibration-damping layer significantly weakens the P2 resonance energy. Moreover, the vibration-damping layer makes the wheel–rail impacts resonate near 60 Hz.

Fig. 19 shows that the vibration-damping layer influences the energy transfer from the wheel–rail system to the track beds across the whole frequency band, and the contribution is more significant below 200 Hz. Specifically, the introduction of the vibration-damping layer increases track bed vibrations by nearly 8.8 dB, reduces energy transmission loss by nearly 11.2 dB, and makes the high-frequency energy distribution of the track beds more uniform. We conclude that laying the vibration-damping layer significantly attenuates wheel–rail impacts and exacerbates track bed vibration.

4.2 Influence mechanism of track bed vibrations on wheel–rail dynamic interaction

From the WRL characteristics under various isolating layer stiffnesses, we conclude that the TBBVs significantly contribute to low-frequency but not

high-frequency WRL. This section discusses the causes of this phenomenon.

4.2.1 Intermodulation effects between the track beds and wheel–rail coupled subsystem

To analyze the influence mechanism of the track bed vibrations on WRL, a modal analysis model for coupling the track beds and wheel–rail coupled subsystem was established by taking the vibration-damping ballastless track as an example (Fig. 20). The interaction between the wheel–rail coupled subsystem and track beds is realized by the fasteners. The intermodulation effects between the track beds and wheel–rail coupled subsystem are shown in Figs. 21 and 22.

P2 resonance is a key mode affecting the WRL. In Fig. 21, compared with the P2 resonance mode (45 Hz) without the influence of track beds, the P2 resonance mode with the influence of track beds is resolved into two vibration modes: in-phase coupling

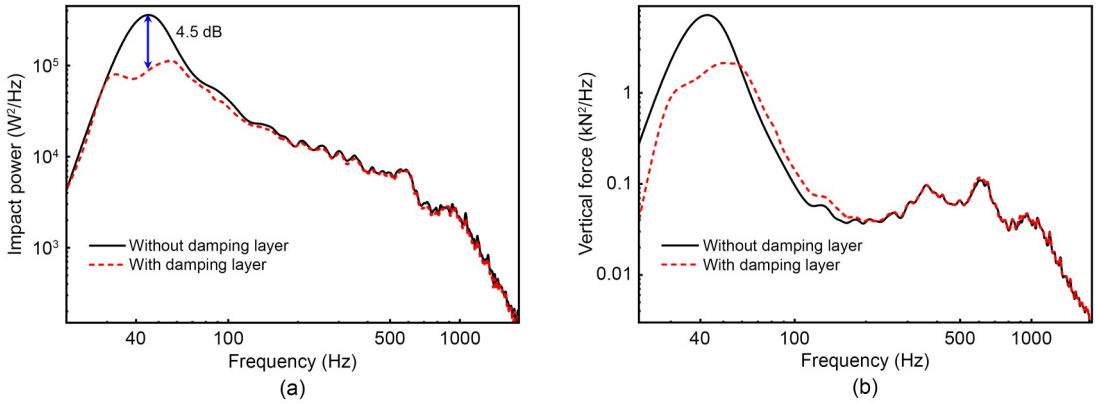

Fig. 18 Influence of the vibration-damping layer on the WRL: (a) impact power; (b) vertical force

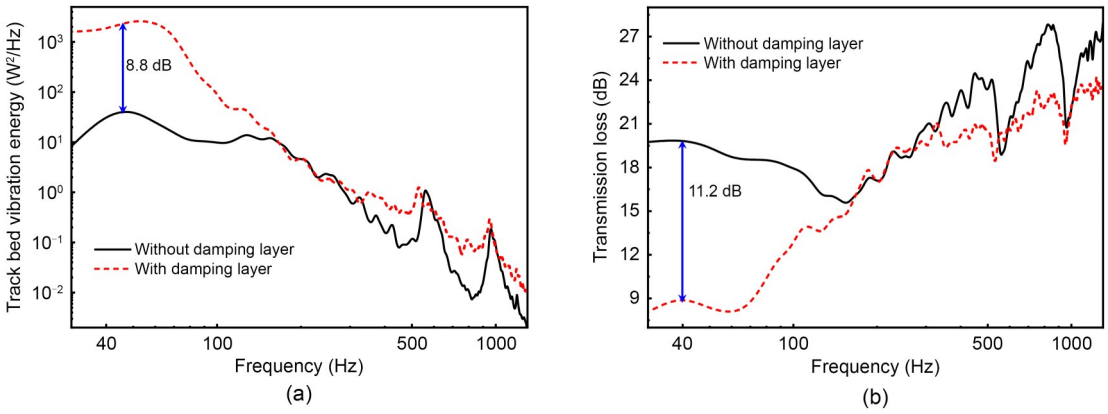

Fig. 19 Influence of the vibration-damping layer on wheel–rail VET: (a) track bed vibration energy; (b) energy transmission loss

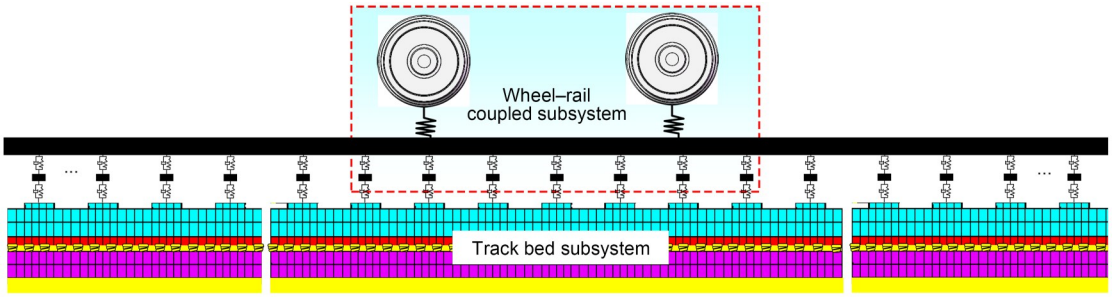

Fig. 20 Mode-coupling model between the track beds and the wheel–rail coupled subsystem

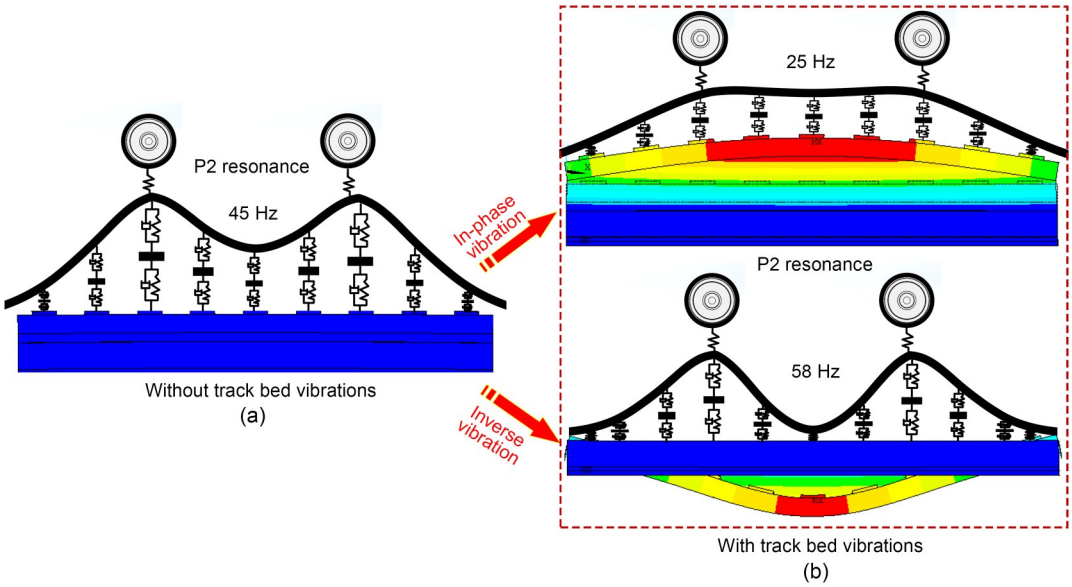

Fig. 21 Wheel–rail P2 resonance mode: (a) without effects of track beds; (b) with effects of track beds

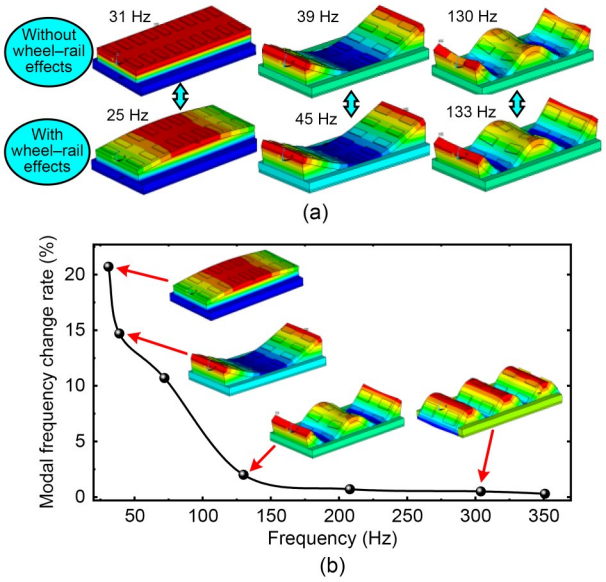

Fig. 22 Track bed modes with effects of the wheel–rail system: (a) difference of track bed modal shapes with and without wheel–rail effects; (b) difference of track bed modal frequencies with and without wheel–rail effects

(25 Hz) and inverse coupling (58 Hz) with the track bed bending vibration. The P2 resonance modal frequency and shape change significantly when considering track bed vibrations, indicating that the wheel–rail coupled vibration modes in the low-frequency range are susceptible to track beds.

In Fig. 22, for a certain track bed mode, the modal frequency with effects of the wheel–rail system compared with that without those effects differs significantly at low frequencies. The difference between the two cases decreases to a negligible level as the modal frequency increases to 200 Hz. This indicates that the track bed modes at high frequencies are less affected by the wheel–rail coupled subsystem.

In summary, the modes of the track bed and wheel–rail coupled subsystem are mutually affected in the low-frequency range, but no mutual effects are observed at high frequencies. Hence, we conclude that the track bed modes and the wheel–rail coupled vibration modes exert intense low-frequency and weak high-frequency intermodulation effects.

4.2.2 Intermodulation effects between the track beds and wheel–rail coupled subsystem

As an example of a vehicle and vibration-damping track, Fig. 23 illustrates the influence of intermodulation effects on the WRL. The coupling resonance of the track bed bending mode with the wheel–rail P2 resonance mode alters the wheel–rail P2 resonance response without mode coupling, causing the WRL to exhibit a new resonance at 58 Hz.

More generally, the frequency range where the track beds and wheel–rail coupled subsystem exert intense intermodulation effects (Figs. 21 and 22) is the same as that where the track bed vibrations significantly affect the WRL (Fig. 23). We infer that, whether the track beds and wheel–rail coupled subsystem produce the intense intermodulation effects is the prerequisite to whether the track bed vibrations

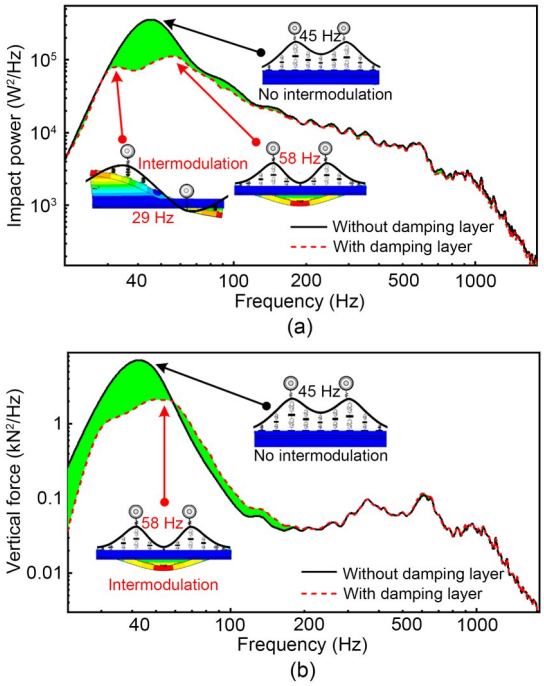

Fig. 23 Influence of intermodulation effects on WRL: (a) impact power; (b) vertical force

change the WRL. If the intermodulation effects are intense, the track bed vibrations significantly alter the WRL, but if they are weak, the track bed vibrations exhibit a moderate effect on the WRL.

Regarding the ballastless tracks in China, although the broadband vibration characteristics of track beds are affected by the track bed type and the stiffness of the isolating layer, intense intermodulation effects of the track beds and wheel–rail coupled subsystem occur mainly below 200 Hz. Consequently, the track bed vibrations make significant contributions to the low-frequency WRL below 200 Hz, but exert only a minor effect on the high-frequency WRL.

4.3 Rational stiffness of isolating layer based on avoiding mode-coupling resonance

The isolating layer stiffness is an important parameter that affects the vibration characteristics of the track beds. To derive the rational stiffness value of the isolating layer, we analyzed the contribution law of the variation of the isolating layer stiffness on the WRL and its VET (Fig. 24).

Fig. 24 shows that with the decrease in isolating layer stiffness, the track bed vibration energy increases slowly and then rapidly, reaching the peak value at 60 MPa/m. Initially, the wheel–rail impact energy

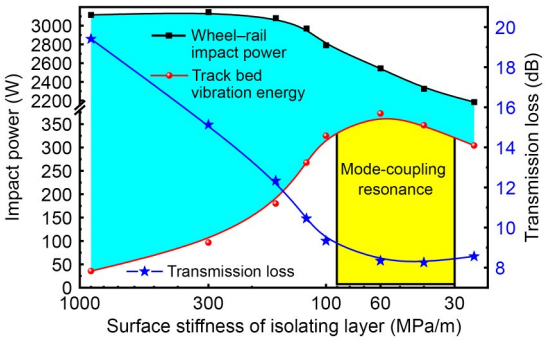

Fig. 24 Contribution of isolating layer stiffness to WRL and its VET

tends to show a gradual reduction but later it decreases rapidly. When the isolating layer stiffness is reduced from 1000 to 60 MPa/m, the wheel–rail impact energy is weakened by only 18%, while the track bed vibration energy is dramatically increased by 9.4 times. This suggests that variations in the isolating layer stiffness have more significant effects on the track bed vibration energy than on the wheel–rail impact energy.

We infer that when the isolating layer stiffness is lower than 90 MPa/m, the wheel–rail system and track beds produce intense intermodulation effects. Fig. 25 shows that when the isolating layer stiffness is 60 MPa/m, the vibration frequency of the track beds is 45 Hz, which is equal to the wheel–rail P2 resonance modal frequency, and the intermodulation effects of the two are the most intense. At this time, the mode-coupling resonance from the track beds to the wheel–rail coupled subsystem is formed and the track bed vibration energy is severe, which may accelerate structural damage to the track. This suggests that the isolating layer stiffness should be selected to avoid the mode-coupling resonance between wheel–rail system and track beds. For the CRTS-III ballastless track, the isolating layer stiffness values of 30–90 MPa/m should be avoided.

5 Conclusions

In this study, we experimentally identified the higher-order modal parameters of track beds and established a vehicle–ballastless track coupled dynamic model that more accurately considers TBBVs. We simulated the WRL and its VET characteristics, investigated the influence of TBBVs on the WRL and its VET, and drew the following main conclusions:

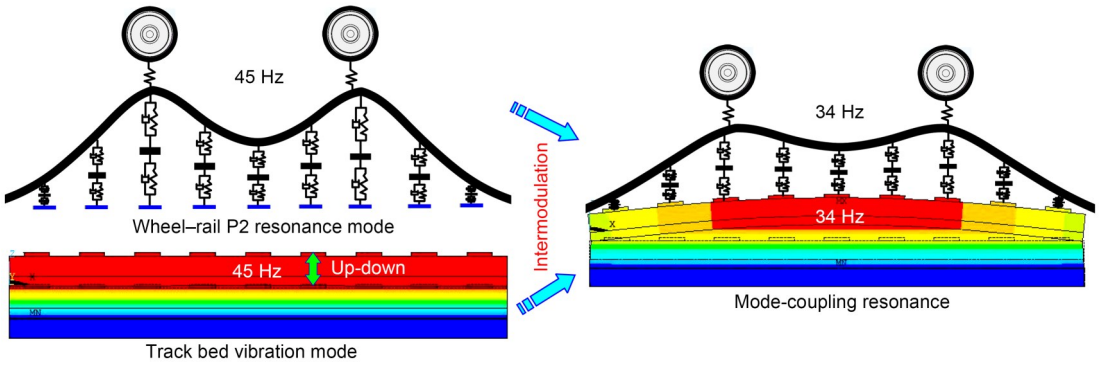

Fig. 25 Mode-coupling resonance between the wheel–rail coupled subsystem and track beds

(1) There are three significant resonances for the wheel–rail impact and track bed vibration energy, with the wheel–rail impact energy resonating around 45, 600, and 1000 Hz, and the track bed vibration energy resonating at 40–80, 530–630, and 850–1000 Hz. The high-frequency resonance peaks of track bed vibration energy are more prominent than those of the wheel–rail impact energy.

(2) The major contribution by TBBVs is to a low-frequency wheel–rail load, and markedly influences its VET across various frequency bands. Installing an isolating cushion and vibration-damping layer significantly enhances the low-frequency vibration energy of the track beds and makes its high-frequency energy distribution more uniform.

(3) The intense intermodulation effects of the track beds and wheel–rail coupled subsystem are the prerequisite for track bed vibrations changing the WRL. Intense low-frequency and weak high-frequency intermodulation effects between the track beds and wheel–rail coupled subsystem were found. The influence of track bed vibrations can be disregarded when focusing only on high-frequency WRLs above 200 Hz.

(4) The more intense the intermodulation effects and mode-coupling resonance of the wheel–rail system and track beds, the more severe the track bed vibration energy. The isolating layer stiffness should be selected to avoid the mode-coupling resonance between the wheel–rail system and track beds. For the CRTS-III ballastless track, the isolating layer stiffness values of 30–90 MPa/m should be avoided.

Acknowledgments

This work is supported by the National Natural Science Foundation of China (No. 52308468), the China Postdoctoral Science Foundation (No. 2022M723390), and the Jiangsu Provincial Excellent Postdoctoral Program (No. 2023ZB020), China.

Author contributions

Chaozhi MA designed the research. Chaozhi MA, Pu WANG, and Bolun AN processed the corresponding data. Chaozhi MA wrote the first draft of the manuscript. Liang GAO and Peng ZHOU helped to organize the manuscript. Liang GAO, Pu WANG, and Mahantesh M NADAKATTI revised and edited the final version.

Conflict of interest

Chaozhi MA, Liang GAO, Pu WANG, Bolun AN, Peng ZHOU, and Mahantesh M NADAKATTI declare that they have no conflict of interest.

References

Aggestam E, Nielsen JCO, 2020. Simulation of vertical dynamic vehicle–track interaction using a three-dimensional slab track model. *Engineering Structures*, 222:110972. https://doi.org/10.1016/j.engstruct.2020.110972

Auersch L, Said S, 2021. Dynamic track-soil interaction—calculations and measurements of slab and ballast tracks. *Journal of Zhejiang University-SCIENCE A (Applied Physics & Engineering)*, 22(1):21-36. https://doi.org/10.1631/jzus.A1900651

Blanco B, Alonso A, Kari L, et al., 2018. Distributed support modelling for vertical track dynamic analysis. *Vehicle System Dynamics*, 56(4):529-552. https://doi.org/10.1080/00423114.2017.1394473

Cai XP, Liang YK, Xin T, et al., 2019. Assessing the effects of subgrade frost heave on vehicle dynamic behaviors on high-speed railway. *Cold Regions Science and Technology*, 158:95-105. https://doi.org/10.1016/j.coldregions.2018.11.009

Chen M, Sun Y, Guo Y, et al., 2019. Study on effect of wheel polygonal wear on high-speed vehicle-track-subgrade vertical interactions. *Wear*, 432-433:102914. https://doi.org/10.1016/j.wear.2019.05.029

Clot A, Romeu J, Arcos R, et al., 2014. A power flow analysis of a double-deck circular tunnel embedded in a full-space.

Soil Dynamics and Earthquake Engineering, 57:1-9. https://doi.org/10.1016/j.soildyn.2013.10.008

El Kacimi A, Woodward PK, Laghrouche O, et al., 2013. Time domain 3D finite element modelling of train-induced vibration at high speed. *Computers & Structures*, 118:66-73. https://doi.org/10.1016/j.compstruc.2012.07.011

Ghangale D, Arcos R, Clot A, et al., 2020. A methodology based on 2.5D FEM-BEM for the evaluation of the vibration energy flow radiated by underground railway infrastructures. *Tunnelling and Underground Space Technology*, 101:103392. https://doi.org/10.1016/j.tust.2020.103392

Gou HY, Gao H, Ban XL, et al., 2023. Vibration energy transmission in high-speed train-track-bridge coupled systems. *Engineering Structures*, 297:117019. https://doi.org/10.1016/j.engstruct.2023.117019

Gupta S, Degrande G, 2010. Modelling of continuous and discontinuous floating slab tracks in a tunnel using a periodic approach. *Journal of Sound and Vibration*, 329(8):1101-1125. https://doi.org/10.1016/j.jsv.2009.10.037

Hu BT, Shan Y, Zhao Y, et al., 2025. Tunneling beneath the pile-raft foundations of high-speed railways: progressive arching deformation and pile settlement behavior. *Underground Space*, in press. https://doi.org/10.1016/j.undsp.2024.12.004

Hussein MFM, Hunt HEM, 2006. A power flow method for evaluating vibration from underground railways. *Journal of Sound and Vibration*, 293(3-5):667-679. https://doi.org/10.1016/j.jsv.2005.12.012

Johansson A, Nielsen JCO, 2007. Rail corrugation growth—influence of powered wheelsets with wheel tread irregularities. *Wear*, 262(11-12):1296-1307. https://doi.org/10.1016/j.wear.2007.01.004

Kalker JJ, 1982. A fast algorithm for the simplified theory of rolling contact. *Vehicle System Dynamics*, 11(1):1-13. https://doi.org/10.1080/00423118208968684

Kaynia AM, Madshus C, Zackrisson P, 2000. Ground vibration from high-speed trains: prediction and countermeasure. *Journal of Geotechnical and Geoenvironmental Engineering*, 126(6):531-537. https://doi.org/10.1061/(ASCE)1090-0241(2000)126:6(531)

Li Q, Li WQ, Wu DJ, et al., 2016. A combined power flow and infinite element approach to the simulation of medium-frequency noise radiated from bridges and rails. *Journal of Sound and Vibration*, 365:134-156. https://doi.org/10.1016/j.jsv.2015.11.041

Ling L, Xiao XB, Xiong JY, et al., 2014. A 3D model for coupling dynamics analysis of high-speed train/track system. *Journal of Zhejiang University-SCIENCE A (Applied Physics & Engineering)*, 15(12):964-983. https://doi.org/10.1631/jzus.A1400192

Ling L, Jiang PB, Wang KY, et al., 2020. Dynamic interaction between rail vehicles and vibration-attenuating slab tracks. *Construction and Building Materials*, 258:119545. https://doi.org/10.1016/j.conbuildmat.2020.119545

Liu C, Xu JM, Wang K, et al., 2022. Numerical investigation on wheel-rail impact contact solutions excited by rail spalling failure. *Engineering Failure Analysis*, 135:106116. https://doi.org/10.1016/j.engfailanal.2022.106116

Luo J, Zhu SY, Zhai WM, 2019. An efficient model for vehicle-slab track coupled dynamic analysis considering multiple slab cracks. *Construction and Building Materials*, 215:557-568. https://doi.org/10.1016/j.conbuildmat.2019.04.219

Luo J, Zhu SY, Zhai WM, 2020. Development of a track dynamics model using Mindlin plate theory and its application to coupled vehicle-floating slab track systems. *Mechanical Systems and Signal Processing*, 140:106641. https://doi.org/10.1016/j.ymssp.2020.106641

Ma CZ, Gao L, Xin T, et al., 2021. The dynamic resonance under multiple flexible wheelset-rail interactions and its influence on rail corrugation for high-speed railway. *Journal of Sound and Vibration*, 498:115968. https://doi.org/10.1016/j.jsv.2021.115968

Ma CZ, Gao L, Xu Y, et al., 2023. Initiation mechanism analysis of wheel polygonal wear on high-speed railway based on refined vibration model for ballastless track system. *Journal of Sound and Vibration*, 559:117782. https://doi.org/10.1016/j.jsv.2023.117782

Martínez-Casas J, Giner-Navarro J, Baeza L, et al., 2017. Improved railway wheelset–track interaction model in the high-frequency domain. *Journal of Computational and Applied Mathematics*, 309:642-653. https://doi.org/10.1016/j.cam.2016.04.034

Mazilu T, 2017. Interaction between moving tandem wheels and an infinite rail with periodic supports–Green's matrices of the track method in stationary reference frame. *Journal of Sound and Vibration*, 401:233-254. https://doi.org/10.1016/j.jsv.2017.04.035

Miao SJ, Gao L, Tong FZ, et al., 2023. Ballastless track mortar layer void detection by high-order statistical analysis of axle box acceleration. *Measurement*, 211:112681. https://doi.org/10.1016/j.measurement.2023.112681

Ni AC, Shi ZF, Meng QJ, 2024. Broadband surface wave attenuation in porous soil by elastic metasurfaces. *International Journal of Mechanical Sciences*, 264:108838. https://doi.org/10.1016/j.ijmecsci.2023.108838

Piotrowski J, Kik W, 2008. A simplified model of wheel/rail contact mechanics for non-Hertzian problems and its application in rail vehicle dynamic simulations. *Vehicle System Dynamics*, 46(1-2):27-48. https://doi.org/10.1080/00423110701586444

Ren JJ, Yan YF, Hu HF, et al., 2019. Analysis method on time-history characteristics of rail supporting force for mixed passenger and freight railway with ballastless track. *Journal of Traffic and Transportation Engineering*, 19(2):82-91 (in Chinese). https://doi.org/10.19818/j.cnki.1671-1637.2019.02.008

Ren JJ, Du JH, Zhang KY, et al., 2024. Transfer relation between subgrade frost heave and slab track deformation and vehicle dynamic response in seasonally frozen ground. *Journal of Zhejiang University-SCIENCE A (Applied Physics & Engineering)*, 25(2):130-146. https://doi.org/10.1631/jzus.A2300303

Sainz-Aja J, Pombo J, Tholken D, et al, 2020. Dynamic calibration of slab track models for railway applications using full-scale testing. *Computers & Structures*, 228:106180. https://doi.org/10.1016/j.compstruc.2019.106180

Sarikavak Y, Goda K, 2022. Dynamic wheel/rail interactions for high-speed trains on a ballasted track. *Journal of Mechanical Science and Technology*, 36(2):689-698. https://doi.org/10.1007/s12206-022-0117-7

Sato Y, 1977. Study on High-Frequency Vibrations in Track Operated with High-Speed Trains. Report No. 1013-76, Railway Technical Research Institute, Tokyo, Japan, p.109-114.

Sheng X, Xiao X, Zhang S, 2016. The time domain moving Green function of a railway track and its application to wheel–rail interactions. *Journal of Sound and Vibration*, 377:133-154. https://doi.org/10.1016/j.jsv.2016.05.011

Song SQ, Zhang WH, Han P, et al., 2018. Sliding window method for vehicles moving on a long track. *Vehicle System Dynamics*, 56(1):113-127. https://doi.org/10.1080/00423114.2017.1346262

Takemiya H, 2003. Simulation of track-ground vibrations due to a high-speed train: the case of X-2000 at Ledsgard. *Journal of Sound and Vibration*, 261(3):503-526. https://doi.org/10.1016/S0022-460X(02)01007-6

Torstensson PT, Squicciarini G, Krüger M, et al., 2019. Wheel–rail impact loads and noise generated at railway crossings–influence of vehicle speed and crossing dip angle. *Journal of Sound and Vibration*, 456:119-136. https://doi.org/10.1016/j.jsv.2019.04.034

Wang S, Xin T, Wang PS, et al., 2023. Novel method for obtaining transfer characteristics of subway-induced ground vibrations. *International Journal of Mechanical Sciences*, 255:108462. https://doi.org/10.1016/j.ijmecsci.2023.108462

Xu L, Zhai WM, 2019. A three-dimensional dynamic model for train-track interactions. *Applied Mathematical Modelling*, 76:443-465. https://doi.org/10.1016/j.apm.2019.04.037

Xu LH, Ma M, Cao RN, et al., 2022. Effect of longitudinally varying characteristics of soil on metro train-induced ground vibrations based on wave propagation analysis. *Soil Dynamics and Earthquake Engineering*, 152:107020. https://doi.org/10.1016/j.soildyn.2021.107020

Xu QY, Sun SW, Xu Y, et al., 2022. Influence of temperature gradient of slab track on the dynamic responses of the train-CRTS III slab track on subgrade nonlinear coupled system. *Scientific Reports*, 12(1):14638. https://doi.org/10.1038/s41598-022-18898-y

Yang XW, Shu Y, Qian DW, et al., 2020. The nonlinear dynamical analysis of damaged concrete slab of high speed railway track using the revised Fourier pseudo-spectral method. *Construction and Building Materials*, 244:118336. https://doi.org/10.1016/j.conbuildmat.2020.118336

Zhai WM, Wang KY, Cai CB, 2009. Fundamentals of vehicle-track coupled dynamics. *Vehicle System Dynamics*, 47(11):1349-1376. https://doi.org/10.1080/00423110802621561

Zhai WM, Jin XS, Wen ZF, et al., 2020. Wear problems of high-speed wheel/rail systems: observations, causes, and countermeasures in China. *Applied Mechanics Reviews*, 72(6):060801. https://doi.org/10.1115/1.4048897

Zhai ZH, Cai CB, Zhu SY, 2023. Implementation of Timoshenko curved beam into train-track-bridge dynamics modelling. *International Journal of Mechanical Sciences*, 247:108158. https://doi.org/10.1016/j.ijmecsci.2023.108158

Zhang KP, Zhang XH, Zhou SH, 2023. Analysis on dynamic behavior of 400 km/h high-speed train system under differential settlement of subgrade. *Engineering Structures*, 278:115521. https://doi.org/10.1016/j.engstruct.2022.115521

Zhang LS, Zhao GT, 2020. Dynamic transfer characteristics of vehicle load on double-block ballastless track of high-speed railway. *Journal of Harbin Institute of Technology*, 52(9):8-16 (in Chinese). https://doi.org/10.11918/201905041

Zheng WQ, Sheng XW, Zhu ZH, et al., 2020. Experimental study on vibration characteristics of unit-plate ballastless track systems laid on long-span bridges using full-scale test rigs. *Sensors*, 20(6):1744. https://doi.org/10.3390/s20061744

Zheng WQ, Sheng XW, Zhu ZH, et al., 2023. Experimental study on vibration characteristics of ballastless tracks on long-span cable-stayed bridge in high speed railway. *China Civil Engineering Journal*, 56(5):79-88 (in Chinese). https://doi.org/10.15951/j.tmgcxb.21121291

Zhu SY, Wang JW, Cai CB, et al., 2017. Development of a vibration attenuation track at low frequencies for urban rail transit. *Computer-Aided Civil and Infrastructure Engineering*, 32(9):713-726. https://doi.org/10.1111/mice.12285